Title
Acquisition and quantification pipeline for in vivo hyperpolarized 13C MR spectroscopy

Journal
Magnetic Resonance in Medicine, 87(4)

ISSN
0740-3194

Authors
Hong, Donghyun
Batsios, Georgios
Viswanath, Pavithra
et al.

Publication Date
2022-04-01

DOI
10.1002/mrm.29081

Peer reviewed

HHS Public Access

Author manuscript

Magn Reson Med. Author manuscript; available in PMC 2023 April 01.

Published in final edited form as:

Magn Reson Med. 2022 April ; 87(4): 1673–1687. doi:10.1002/mrm.29081.

Acquisition and quantification pipeline for *in vivo* hyperpolarized ^{13}C magnetic resonance spectroscopy

Donghyun Hong, **Georgios Batsios**, **Pavithra Viswanath**, **Anne Marie Gillespie**, **Manushka Vaidya**, **Peder E.Z. Larson**, **Sabrina M. Ronen**

Department of Radiology & Biomedical Imaging, University of California San Francisco, San Francisco, CA

Abstract

Purpose—The goal of this study was to combine a specialized acquisition method with a new quantification pipeline to accurately and efficiently probe the metabolism of hyperpolarized ^{13}C-labeled compounds *in vivo*. In this study, we tested our approach on [2-^{13}C]pyruvate and [1-^{13}C]α-ketoglutarate data in rat orthotopic brain tumor models at 3 T.

Methods—We used a multiband metabolite-specific RF excitation in combination with a variable flip angle scheme to minimize substrate polarization loss and measure fast metabolic processes. We then applied spectral-temporal denoising using singular value decomposition to enhance spectral quality. This was combined with LCModel-based automatic ^{13}C spectral fitting and flip angle correction to separate overlapping signals and rapidly quantify the different metabolites.

Results—Denoising improved the metabolite signal-to-noise ratio (SNR) by approximately 5. It also improved the accuracy of metabolite quantification as evidenced by a significant reduction of the Cramer Rao Lower bounds. Furthermore, the use of the automated and user-independent LCModel-based quantification approach could be performed rapidly, with the kinetic quantification of 8 metabolite peaks in a 12-spectrum array achieved in less than one minute.

Conclusion—The specialized acquisition method combined with denoising and a new quantification pipeline using LCModel for the first time for hyperpolarized ^{13}C data enhanced our ability to monitor the metabolism of [2-^{13}C]pyruvate and [1-^{13}C]α-ketoglutarate in rat orthotopic brain tumor models *in vivo*. This approach could be broadly applicable to other hyperpolarized agents both preclinically and in the clinical setting.

Keywords

Hyperpolarized ^{13}C MRS; Brain tumor; Multiband excitation; Denoising; LCModel; Variable flip angle correction

[*]**Address for correspondence:** Sabrina M. Ronen, Ph.D., Department of Radiology and Biomedical Imaging, University of California San Francisco, 1700 4th St., Suite 303 Box 2532, San Francisco, CA 94158, Tel: +1 415 514 4839, sabrina.ronen@ucsf.edu.
Author Donghyun Hong and author Georgios Batsios contributed equally to this work.
Author Peder E.Z. Larson and author Sabrina M. Ronen contributed equally to this work.

Introduction

Hyperpolarized (HP) carbon 13 (^{13}C) magnetic resonance spectroscopy (MRS) in combination with the dissolution-Dynamic Nuclear Polarization (d-DNP) technique, which leads to a signal-to-noise ratio (SNR) enhancement for ^{13}C of over 10,000 fold, is a novel approach to monitor real-time metabolism non-invasively.[1,2] This technique makes it possible to investigate a wide range of biochemical processes that are relevant to human disease. For example, HP [1-^{13}C]pyruvate, [2-^{13}C]pyruvate, and [1-^{13}C]α-ketoglutarate (αKG) have been developed and used to investigate cancer,[3–7] ischemia,[8] cardiac diseases,[9] and diabetes.[10] The method has been used to characterize important biological processes including the Warburg effect and tricarboxylic acid (TCA) cycle metabolism,[6,11–15] and to monitor response to treatment.[16–18] Importantly, HP ^{13}C MRS is now in clinical trials to assess metabolism, detect disease, and monitor treatment response in patients.[19–21]

Favorable spectral quality is a prerequisite to accomplishing the fundamental goal of HP ^{13}C MRS and reliably monitoring metabolism. Although the hyperpolarization technique provides a significant SNR enhancement,[1] HP *in vivo* spectroscopy acquisition can be challenging because the hyperpolarized signal decays rapidly as a result of T_1 relaxation and RF excitation. Fast acquisition strategies have helped in this regard and continue to be developed.[22,23] Another potential challenge is data analysis. In the case of [1-^{13}C]pyruvate, which is currently the most commonly used HP agent, several data analysis methods have been considered and used.[24,25] However, for other agents such as [2-^{13}C]pyruvate, the low concentration of product and signal overlap associated with insufficient B_0 field and poor shimming make it difficult to monitor metabolic conversions accurately. Specialized acquisition and precise quantification methods together with additional processing steps are therefore required as the field moves beyond HP [1-^{13}C]pyruvate.

In our laboratory, we have focused on using HP ^{13}C MRS to characterize and monitor brain tumors. We have assessed the metabolic reprogramming associated with tumor development and its modulation with treatment in both high-grade glioblastomas (GBM) and low-grade gliomas (LGGs).[26–28] Most notably, we have shown the value of HP [2-^{13}C]pyruvate and HP [1-^{13}C]αKG. HP [2-^{13}C]pyruvate detects glutamate production that reflects the metabolic reprogramming that occurs in LGG.[5] HP [1-^{13}C]αKG detects glutamate production[29] as well as production of the oncometabolite 2-hydroxyglutarate (2HG) that results from the LGG driver mutation in isocitrate dehydrogenase 1 (IDH1).[3] However, our previous studies used different acquisition schemes tailored to improve detection of the different products of HP [1-^{13}C]αKG at a clinical 3 T scanner, and the data analysis was manual and time-consuming.

Here we describe a specialized acquisition method with a new quantification pipeline, which we have used to investigate the *in vivo* metabolism of HP [2-^{13}C]pyruvate and [1-^{13}C]αKG in rat tumor models in a dedicated preclinical 3 T scanner. Data was acquired using a multiband, metabolite-specific RF excitation[30,31] in combination with a variable flip angle (VFA) scheme[32–34] to minimize substrate polarization loss and measure fast metabolic processes. We then used spectral-temporal denoising to enhance spectral quality, an LCModel-based automatic spectral fitting, to our knowledge for the first time for

hyperpolarized ^{13}C data, and flip angle correction to separate overlapping signals and monitor metabolic kinetics. Collectively, our approach enhanced our ability to rapidly monitor metabolism *in vivo*.

Methods

1. Animal Models

All animal studies were carried out under Institutional Animal Care and Use Committee approval. Orthotopic brain tumor xenografts were generated in twelve 100 – 150 g male nude rats (Charles River CD®) by intracranial injection of ~3×10^5 cells as previously described.[35] Five animals were implanted with genetically engineered mutant IDH1 U87 (U87IDHmut) cells,[36] three animals with BT257 mutant IDH1 astrocytoma cells,[37] and two with U87 GBM cells that are IDH1 wild-type. Animals were monitored for 6 – 8 weeks for the U87IDHmut and U87 animals and 12 – 14 weeks for the BT257 animals at which point tumor volume reached ~0.22 cm^3.

2. ^{13}C substrate preparation and hyperpolarization

HP substrates were prepared as previously described.[3,14] Briefly, [2-^{13}C]pyruvic acid (Sigma-Aldrich, MO) was mixed with 15 mM OX63 trityl radical (Oxford Instruments, UK) and 1.5 mM of Dotarem (Guerbet, France). [1-^{13}C]α-ketoglutaric acid (Sigma-Aldrich, MO) was dissolved in a 3:1 mixture of water and glycerol, with 17.3 mM of OX63 trityl radical and 0.4 mM of Dotarem. A volume of 48 μl ([2-^{13}C]pyruvic acid) or 60 μl ([1-^{13}C]α-ketoglutaric acid) was polarized using a Hypersense polarizer (3.35 T, 1.4 K, Oxford Instruments, UK) for approximately 45 and 90 mins, respectively. Following polarization, the sample was immediately dissolved in 4 ml of Tris-based isotonic buffer (40 mM Tris-HCl (pH = 8), 3 μM ethylenediaminetetraacetic acid (EDTA), 200 mM NaOH) and used for the *in vivo* experiments.

3. Metabolite-specific RF pulse design

The RF pulse was designed using an in-house software package in Matlab (ver. 2019b, Mathworks, MA) available online (https://github.com/LarsonLab/hyperpolarized-mri-toolbox).[38] The RF pulses were designed to increase the SNR from the metabolic products while minimizing the depolarization of the HP substrate. For [2-^{13}C]pyruvate, we designed a two-band flyback spectral-spatial (SPSP) RF pulse for a 10 mm slab with 1.02 ms duration, 0.2336 G peak amplitude, a gradient amplitude of 10.10 G/cm, and a maximum slew rate of 555.6 G/cm/ms (Figure 1A and B). The response of the RF pulse was specified for the following resonances and bandwidths at 3 T: (1) 207.8 ppm ± 1 ppm ([2-^{13}C]pyruvate) with 0.01 % ripple and 4° flip angle, and (2) 183.9 ppm ± 1 ppm ([5-^{13}C]glutamate) with 0.01 % ripple and 30° flip angle. A minimum-phase spectral filter was used to reduce the pulse duration and peak power. The simulated spectral performance of the pulse over different frequencies and spatial positions as well as the pulse profile at the center of the slab can be seen in Figures 1C and 1D, respectively. The spatial excitation profile for the frequency bands of [2-^{13}C]pyruvate and [5-^{13}C]glutamate and the frequency in the center of the [2-^{13}C]lactate doublet are shown in Supporting Information Figures S1A–C.

For [1-^{13}C]αKG, we designed a three-band SPSP RF pulse for a 12 mm slab with 8.31 ms duration, 0.1639 G peak amplitude, a gradient amplitude of 12.97 G/cm, and a maximum slew rate of 555.6 G/cm/ms (Supporting Information Figures S2A and B). The response of the RF pulse was specified for the following resonances and bandwidths at 3 T: (1) 172.6 ppm ± 1 ppm ([1-^{13}C]αKG) with 0.005 % ripple and 2° flip angle, (2) 177.5 ppm ± 1 ppm ([1-^{13}C]glutamate) with 0.01 % ripple and 25° flip, and (3) 184 ppm ± 1 ppm ([1-^{13}C]2HG) with 0.01 % ripple and 25° flip angle. A minimum-phase spectral filter was used to reduce the pulse duration and peak power. The simulated spectral performance of the pulse over different frequencies and spatial positions, as well as the pulse profile at the center of the slab and the spatial excitation profile for the frequency bands of [1-^{13}C]αKG, [1-^{13}C]glutamate, and [1-^{13}C]2HG, can be seen in Supporting Information Figure S2C–F.

The relative flip angles between substrate and products were chosen empirically based on prior experience with [2-^{13}C]pyruvate[21] and with [1-^{13}C]αKG.[3,29] Additionally, we incorporated progressively increasing flip angles between excitations designed to improve the expected SNR of the metabolites by accounting for T_1 relaxation and prior RF excitations. The product flip angles were designed with the maximum total SNR flip angle formulation from Equation (8) in Nagashima.[39] For [2-^{13}C]pyruvate studies, the applied flip angle on [5-^{13}C]glutamate was designed using T_1 = 30 s and TR = 3 s, resulting in a progressive increase from 26.52° to 90.00° over 12 repetitions, while the [2-^{13}C]pyruvate flip angle went from 3.84° to 13.04°. For [1-^{13}C]αKG studies, the applied flip angle for [1-^{13}C]glutamate and [1-^{13}C]2HG was designed using T_1 = 26 s and TR = 6 s, resulting in a progressive increase from 38.01° to 90.00° over 8 repetitions, while the [1-^{13}C]αKG flip angle went from 3.04° to 7.20°. For full list of flip angles see Supporting Information Table S1.

The SPSP RF pulse performance, as well as the accuracy of the variable flip angle scheme, were tested using a 2.4 cm spherical phantom filled with 5 M thermally polarized [1-^{13}C]urea placed in the isocenter of a horizontal 3 T preclinical MRI system (Bruker BioSpec 105 mm bore diameter, Germany). A linear dual-tuned ^{1}H-^{13}C volume coil (42 mm inner diameter, Bruker, Germany) was used for the acquisitions. In order to get representative data for the behavior of the pulse at each specified frequency band, the transmitter offset was shifted. The RF pulse peak power was calibrated manually to produce a 90° at the transmitter offset frequency corresponding to [5-^{13}C]glutamate ([2-^{13}C]pyruvate pulse) or [1-^{13}C]2HG and [1-^{13}C]glutamate ([1-^{13}C]αKG pulse).

4. Data Acquisition

Animals were anesthetized using 1–2 % isoflurane in O_2 and a tail vein catheter placed. Animals were then injected intraperitoneally with 100 mg/kg ketamine plus 10 mg/kg xylazine and placed head first in the prone position. Animals were monitored using an animal respiratory monitoring device (MR-compatible Small Animal Monitoring, SA Instruments, USA).

All studies were performed using a Biospec 3T pre-clinical MR scanner (Bruker, Germany). First, T_2-weighted images of the rat brain were acquired using a dual-tuned ^{1}H/^{13}C volume coil (42 mm inner diameter, Bruker, Germany) and a multi-slice spin-echo sequence with the

following parameters: TE = 64 ms, TR = 3484 ms, matrix = 256 × 256, resolution = 0.13 × 0.13 mm^2, slice thickness = 1 mm, and the number of averages = 5.

A spectroscopy slab was then located across the axial plane covering the whole tumor region (See Supporting Information Figure S3). The spectroscopic slab was shimmed using a B_0 map-based shim and local shim sequences provided by Bruker. Hyperpolarized substrates were then injected through the tail vein over ~12 s and 1D dynamic slab spectroscopy data acquired using the above-mentioned pulse sequences and the following parameters for [2-^{13}C]pyruvate and [1-^{13}C]αKG, respectively: slab thickness = 10 and 12 mm, data points = 1024, spectral bandwidth = 300 ppm and 50 ppm, number of repetitions = 12 and 8, temporal resolution = 3 s and 6 s. Data acquisition started at the start of the injection for [2-^{13}C]pyruvate and after 11 s for [1-^{13}C]αKG in order to preserve substrate magnetization and increase the accumulated product signal.

5. Spectral fitting performance assessment

The spectral fitting performance was assessed using simulated spectra with various SNR levels to find an association between SNR and quantification precision and identify a thresholding SNR for stable quantification. The simulated spectra were comprised of three peaks at an intensity ratio of 20:2:1, representing a large substrate peak and two smaller product peaks. Various levels of noise, which were measured from our acquired *in vivo* spectra to mimic a realistic range of SNR, were then added to the simulated spectrum in the time domain using a custom-written Matlab script. The resulting spectra had SNR values from 5 to 3000. Spectra were then fit using a corresponding basis-set in LCModel (Provencher, Canada)[40,41], and the quantified signals and their corresponding Cramer Rao Lower Bounds (CRLBs) assessed as a function of SNR. The basis set was simulated using NMRSIM in the Topspin suite (version 4.0, Bruker, Germany).

6. Pre-processing

The SNR of the acquired *in vivo* signal was improved by using Singular Value Decomposition (SVD)[42]. According to the SVD theorem, we can factorize a two-dimensional matrix M of the acquired *in vivo* spectrum over time into the product of three matrices as follows:

$$M = \sigma_1 u_1 v_1^T + \sigma_2 u_2 v_2^T + \ldots + \sigma_n u_n v_n^T = \mathrm{U}\Sigma V^T \quad (1)$$

where M is the data matrix of size $m*n$ (i.e., spectral points * time points), U is an $m*m$ orthonormal matrix, Σ is an $m*n$ diagonal matrix of singular values, and V is an $n*n$ orthonormal matrix. In this study, m = 1024 and n = 12 and 8 for [2-^{13}C]pyruvate and [1-^{13}C]αKG, respectively. After factorization, components with the highest singular values are mostly signal while those with the lowest values are mostly noise. Assuming that the metabolite signals and noise signal have low cross-correlation[43] and that the noise is white Gaussian,[44,45] dimensionality reduction can be achieved by simply dropping columns. Therefore, when the rank order of this dimensionality reduction is optimally selected, the summation of the high-ranked singular vectors can ideally reconstruct noise-free time-resolved spectra whereas the low-ranked singular vectors mostly contain noise. We tested

various rank orders from 5 to 9 for [2-^{13}C]pyruvate and from 2 to 5 for [1-^{13}C]αKG. Then, for each animal, an optimal rank value was manually selected which showed the highest SNR while detecting all the expected metabolites based on prior knowledge of metabolic pathways. After the SVD denoising, 0.5 Hz apodization using the Lorentzian lineshape was additionally applied to remove high-frequency noise in the frequency domain. Spectral quality improvement was evaluated by SNR measurement (substrate peak amplitude to the standard deviation of the noise ratio).

7. LCModel fitting

Metabolite concentrations for each spectrum were quantified using LCModel. The basis set included ^{13}C-labeled carbon moieties in substrates and expected ^{13}C-labeled carbon moieties in products as well as natural abundance ^{13}C carbonyls with sufficiently long T_1 values to be detected in our spectra. The T_1 relaxation time of each carbon was also taken into consideration in simulations to consider the T_1 induced amplitude differences between metabolites (Supporting Information Table S2). Accordingly, for data obtained with HP [2-^{13}C]pyruvate, the basis set was comprised of [2-^{13}C]pyruvate, [1-^{13}C]pyruvate, [1-^{13}C]acetoacetate, [1-^{13}C]acetyl-carnitine, [2-^{13}C]pyruvate-hydrate, [5-^{13}C]glutamate, [5-^{13}C]glutamine, and [2-^{13}C]lactate. For data obtained with HP [1-^{13}C]αKG, the basis set was comprised of [1-^{13}C]αKG, [1-^{13}C]glutamate, [1-^{13}C]αKG-hydrate, and [5-^{13}C]αKG + [1-^{13}C]2HG (because the two resonances are only 0.1 ppm apart and cannot be resolved *in vivo*[3]). However, in order to also take into consideration possible asymmetry of doublets due to the natural abundance of [1,2-^{13}C] pyruvate[46] or the inconsistent flip angle of the SPSP pulse, we estimated the intensity ratio between upfield and downfield peaks for [1-^{13}C]pyruvate and [2-^{13}C]lactate. After comparing the signal intensity differences, we found that the downfield to upfield ratio was approximately 1.02 and 0.80 for the [1-^{13}C]pyruvate and [2-^{13}C]lactate doublets, respectively (See Supporting Information Figure S4).We proceeded to design a basis set that takes into account these intensity differences. Since LCModel is mainly designed to quantify proton spectroscopic data, parameter modifications were required to quantify the ^{13}C data. First, the chemical shifts of the *in vivo* spectra and fitting models were down-scaled fifty times by modifying the dwell-time to create a similar chemical shift range to that of proton spectroscopy, and the substrate peaks, [2-^{13}C]pyruvate and [1-^{13}C]αKG, were positioned at 4.65 ppm, which is the water resonance frequency that LCModel uses as a reference.[41] In addition to the chemical shift rescaling, additional modifications of the LCModel control parameters were implemented including the exclusion of the macromolecule/lipid signal and the use of a restricted baseline estimation. The full description of the modified parameters and values is listed in Supporting Information Table S3. Spectral quality and spectral fitting quality were evaluated using SNR and CRLB, respectively. We excluded metabolites with CRLB values of 999 %, which indicates that the metabolite was not detected. The significance of CRLB differences between the pre- and post-processing were compared using a paired Student's t-test. A paired t-test was also used to assess the significance of [5-^{13}C]αKG + [1-^{13}C]2HG signal increase at 38 s. A p-value of less than 0.05 was considered statistically significant.

Since LCModel provides automated 0th and 1st order phase corrections during the quantification steps, we did not perform any additional phase correction. However, for

the [2-^{13}C]pyruvate data, LCModel could not simultaneously phase all the metabolites in the spectrum because the SPSP RF excitation profile led to complex phase distortions (when [2-^{13}C]pyruvate is in phase, [1-^{13}C]pyruvate, [1-^{13}C]acetoacetate, [1-^{13}C]acetyl-carnitine, [5-^{13}C]glutamate, [5-^{13}C]glutamine are out of phase). To address this challenge, the LCModel analysis was performed in two steps. In the first step, we quantified the three large metabolites: [2-^{13}C]pyruvate, [2-^{13}C]pyruvate-hydrate, and [2-^{13}C]lactate using the full chemical shift. In the second step, we cropped the chemical shift range to 70 – 190 ppm and quantified [1-^{13}C]pyruvate, [1-^{13}C]acetoacetate, [1-^{13}C]acetyl-carnitine, [2-^{13}C]pyruvate-hydrate, [5-^{13}C]glutamate, [5-^{13}C]glutamine, and [2-^{13}C]lactate. Metabolite concentrations in the two different steps were scaled by the commonly quantified metabolites: [2-^{13}C]lactate and [2-^{13}C]pyruvate-hydrate.

8. Variable Flip Angle correction

The VFA scheme chosen has a clear advantage in that it creates a consistent signal level with relatively high SNR by compensating for the signal losses due to both RF excitation and T_1 decay. Nonetheless, the increasing flip angles can obscure metabolite kinetics. To determine metabolite kinetics we, therefore, corrected for the variation in signal intensity due to the VFA as follows:

$$C_{corr}(n) = C_{meas}(n) * sin(\theta_{last})/sin(\theta_n) \quad (2)$$

Where $C_{corr}(n)$ is the corrected metabolic concentration, $C_{meas}(n)$ is the measured metabolic concentration that was quantified with LCModel and θ is the flip angle. The flip angles of each pulse are shown in Supporting Information Table S1.

Supporting Information Figure S4 illustrates a flow chart of the acquisition and quantification steps used in this study.

Results

Initially, the spectral fitting performance was assessed using simulated spectra with various SNR levels. Figure 2A illustrates three representative LCModel results with residual signal (i.e. the difference between the measured and the fitted spectra) for spectra of different SNR levels that included one large ‘substrate’ peak and two smaller ‘product’ peaks. When we quantified the peaks and their corresponding CRLBs (Figure 2B), we found that as long as the spectral SNR is over approximately 10 each peak was quantified consistently with a CRLB below 5% (see Figure 2C).

Figure 3 shows a comparison of unprocessed (A and B) and SVD processed (C and D) spectra acquired over time from the rat brain following [2-^{13}C]pyruvate (A and C) and [1-^{13}C]αKG (B and D) injections. Supporting Information Figure S4 shows the average SNR of metabolites observed following [2-^{13}C]pyruvate injection into U87IDHmut tumor-bearing rats (A) and [1-^{13}C]αKG injection into BT257 (B) and U87 (C) tumor-bearing rats before and after denoising. The selected denoising ranking order was between 6 and 7 for [2-^{13}C]pyruvate and was between 3 and 5 for [1-^{13}C]αKG depending on the animal. On average the substrate peak SNR across all time points and subjects increased from 318.06 ±

70.23 ([2-^{13}C]pyruvate injection into U87IDHmut rats), 155.98 ± 22.24, and 166.18 ± 28.56 ([1-^{13}C]αKG injection into BT257 and U87 rats, respectively) before denoising to 1507.58 ± 322.72, 698.01 ± 134.25, and 651.83 ± 72.29 after denoising resulting in improved detection of low concentration metabolites.

Examples of LCModel fit results for the post-denoised spectra are illustrated in Figure 4 in spectra recorded post substrate injection at 24 s ([2-^{13}C]pyruvate in A, B) and at 32 s ([1-^{13}C]αKG in C) when all product metabolites are clearly visible. As mentioned above, due to the challenge of phasing the whole spectrum following [2-^{13}C]pyruvate injection, the three large metabolites ([2-^{13}C]pyruvate, [2-^{13}C]pyruvate-hydrate, and [2-^{13}C]lactate) were quantified in the full spectrum first (Figure 4A). [2-^{13}C]pyruvate was then excluded allowing phasing and LCModel fitting for all other metabolites (Figure 4B). The enlarged area of Figure 4B illustrates that LCModel was able to quantify overlapping metabolites with relatively lower concentrations. The [1-^{13}C]αKG spectra are relatively simpler than those of [2-^{13}C]pyruvate and not surprisingly LCModel was able to fit all the metabolites in this case as well. Importantly, the analysis of all twelve spectra acquired following [2-^{13}C]pyruvate injection required less than one minute for both the denoising and fitting steps under our Linux environment (Intel Xenon E5–1620 quadcore 3.6 GHz CPU and 32 GB RAM).

Figure 5 compares the goodness of fit as evaluated by the mean CRLB of LCModel fitting when comparing pre- and post-denoised spectra over all time points. Denoised spectra showed significantly improved fitting precision in comparison with unprocessed spectra for all metabolites except [2-^{13}C]pyruvate, [1-^{13}C]pyruvate, and [1-^{13}C]αKG for which fitting precisions between pre- and post-denoised spectra are comparable due to their relatively high SNR prior to denoising.

VFA correction results are shown in Figure 6. Figure 6A shows expected magnetization variations over the increased flip angle that were used to estimate the flip angle correction factors. Figures 6B and C illustrate the impact of the VFA correction for representative metabolites obtained following injection of [2-^{13}C]pyruvate and [1-^{13}C]αKG. The results highlight the value of the VFA acquisition method which maintains a high signal by increasing the flip angle over time and the value of using the VFA correction factors for the estimation of true metabolite kinetics.

Figure 7 compares average metabolite kinetics as estimated using the LCModel fitting and VFA correction between pre-denoised and post-denoised spectra over time for [2-^{13}C]pyruvate and [1-^{13}C]αKG. Denoised data showed improved performance in terms of consistency and clarity. Whereas quantified metabolites between pre- and post-denoised spectra are comparable for the substrate metabolites, the denoised spectra of low concentration metabolites show smoother metabolic kinetics for both substrates. In addition, the smaller error bars for most of the denoised metabolites indicate that the denoising step improves spectral quantification in terms of consistency. The improved data quality also allowed for a clearer detection of metabolism. Figures 7B and C show the fate of [1-^{13}C]αKG in BT257 tumors, which are IDH mutant, and U87 tumors that are IDH wild-type. Of note is that the [5-^{13}C]αKG + [1-^{13}C]2HG signal in the BT257 shows a

significant increase ($p < 0.05$) at 38 s. This increase is consistent with our previous work demonstrating that it reflects the production of 2HG.[3] In contrast, in the case of the U87 tumors, only the monotonic signal decay of [5-^{13}C]αKG (which resonates at 0.1ppm away from [1-^{13}C]2HG[3]) is observed, which is consistent with the absence of the IDH mutation and 2HG production. We also observed the production of [1-^{13}C]glutamate, reflecting the alternate metabolic fate [5-^{13}C]αKG as previously reported.[29]

Discussion

Non-invasive detection of enzymatic activities and their modulation in response to therapy are critical for our understanding of cancer biology and the detection and monitoring of cancer patients. ^{13}C MRS in combination with the hyperpolarization technique makes it possible to monitor real-time *in vivo* metabolism by overcoming the low gyromagnetic ratio of ^{13}C (its γ is approximately one-fourth that of protons). However, challenges remain, due to the limited SNR of some metabolic products and the rapid loss of the HP signal associated with T_1 relaxation time and RF excitation. The T_1 of HP carbonyls, which are the most commonly labeled carbon moieties, benefit from lower field strengths. However, this can also limit the chemical shift dispersion between compounds. This is not the case for [1-^{13}C]pyruvate, which is the most widely used HP agent and now in clinical trials: the chemical shift separation between [1-^{13}C]pyruvate and its metabolic products lactate and bicarbonate is sufficiently high[2]. However, signal overlap can present a challenge for the development and translation of other HP agents such as [2-^{13}C]pyruvate, [1-^{13}C]glutamic acid, or γ-glutamyl-[1-^{13}C]glycine.[14,47–49] Specialized acquisition and quantification strategies are therefore needed to achieve the best possible information from HP ^{13}C data.

A commonly used acquisition scheme is multi-band, metabolite-specific excitation,[50] which uses a relatively low flip angle for the substrate peak, to preserve its non-reusable magnetization, and a higher flip angle to acquire the relatively smaller product signals. At the same time, a steadily increasing VFA scheme uses progressively increasing amounts of the magnetization as it decays over the course of the experiment.[25,32] The combination of these two approaches has been applied previously by our group for monitoring either the conversion of HP [1-^{13}C]αKG to [1-^{13}C] 2HG or the conversion of HP [1-^{13}C]αKG to [1-^{13}C]glutamate on a 3T clinical MR system.[3,29] In this study, we report for the first time the application of these methods for the simultaneous monitoring of [1-^{13}C]2HG and [1-^{13}C]glutamate production from HP [1-^{13}C]αKG in a single pulse sequence. Further studies are underway to further improve upon this sequence to allow greater signal localization using echo-planar spectroscopic imaging. However, the presented study confirms our ability to simultaneously monitor the fate of HP [1-^{13}C]αKG to both of its downstream metabolites informing the status of mutant IDH1.[3,29] The difference in location and shape of the slices observed in the case of [2-^{13}C]pyruvate and its products is due to chemical shift misregistration that commonly occurs in SPSP pulses and leads to shifted slice locations as a function of frequency. Although this limits the utility of our current pulse for accurately monitoring [2-^{13}C]pyruvate metabolism, this limitation was addressed when we created the SPSP pulse for [1-^{13}C]αKG through an additional design step that allows for some correction of the chemical shift slice misregistration.[31 38] In the current study, our

main goal was to investigate the ability of denoising to improve the detection of metabolites with low SNR. Future studies investigating the specifics of [2-^{13}C]pyruvate metabolism will utilize a modified pulse to more accurately probe pyruvate metabolism.

Despite the specialized acquisition schemes and the signal enhancement provided by d-DNP, some of our product signals have relatively low intensities. To address this challenge, we applied a denoising method to improve spectral SNR. SVD can be used to extract the primarily signal information from the noise by reducing the rank order without introducing broadened linewidths.[42] SVD denoising of our data resulted in ~5 times improved overall SNR for all the metabolites. Recently, Brender *et al.*[51] reported that they achieved an approximately 7 fold SNR gain using the SVD method in the thermally polarized ^{13}C data, which was acquired with 4500 scans over an hour. Their SNR improvement using the same denoising method is in line with our findings. Although recent 2D spectroscopic imaging studies reported that higher-order denoising methods using Tensor denoising[51,52] could also be used to improve the SNR, such approaches cannot be applied to our 1D time-resolved spectral results that are composed of spectral and temporal data. Most importantly, denoising helped monitor low concentration metabolic products which were not clearly visible prior to denoising and therefore improved our ability to monitor metabolism.

The ^{13}C spectrum has a relatively large chemical shift range compared to the proton spectrum, and a relatively small number of metabolites are observed in the HP spectrum. Nonetheless, the quantification of overlapping signals can be time-consuming and subject to variation. More robust and rapid metabolite quantification can be achieved using spectral model fitting based on prior knowledge. Here, we used LCModel fitting, which is one of the most widely used approaches for the analysis of proton MRS data. We chose this method for several reasons including 1) reliable spectral fitting performance, 2) fully automated batch processing, 3) embedded 0^{th} / 1^{st} order phase, lineshape, and baseline corrections, 4) goodness of fit evaluation and 5) easy modification of control parameters for use with non-proton spectra. Others have shown the feasibility of using LCModel fitting for ^{13}C[53] and ^{31}P[54] data. In particular, Henry *et, al.*[53] quantified the ^{13}C spectrum using LCModel but implemented extensive modifications. In our study, we used an alternate and simpler approach. Because the peaks of the HP ^{13}C spectrum are relatively well separated, we modified the dwell time and the basis set to the chemical shift range of the proton spectrum. This simple approach allowed us to leverage all the features included in LCModel without changing multiple LCModel control parameters. To the best of our knowledge, this is the first use of LCModel for the analysis of HP ^{13}C data. Importantly, this approach also resulted in rapid data analysis with quantification of our spectral array achieved in less than one minute. This rapid quantification pipeline could also be easily scaled to 2D and 3D spectroscopic data.

CRLB, which is defined as the lowest possible standard deviation of all unbiased model parameter estimates obtained from the *in vivo* data,[41] is used as a parameter to evaluate spectral quality. In proton spectroscopy, CRLB values under 50% are considered as acceptable and values under 20% are considered good.[55] A previous study has shown that increased fitting precision leads to smaller standard deviations and therefore consistent and comparable quantification.[56] Since the carbon data is much simpler than that of proton

and it is not associated with a complicated baseline, we expect lower CRLB values for the carbon data. According to our simulation results which mimic the *in vivo* data, when the peak SNR is over 10, its corresponding CRLB is typically below 5% and under those circumstances, LCModel showed stable and consistent quantification performance. Since the CRLB is closely related to the level of residual signal after fitting,[57] decreased noise level by denoising necessarily improves fitting precision. In our study, most metabolites had adequate SNR after denoising resulting in higher fitting precision, and post-processed data showed smooth dynamic curves with smaller standard deviations.

[2-^{13}C]pyruvate is a useful agent to assess the TCA cycle, which is a key pathway involved in energy metabolism in the brain. A previous study has shown the dynamic conversion of the HP [2-^{13}C]pyruvate to [2-^{13}C]lactate and [5-^{13}C]glutamate in the rat[7,14] and human[21] brain. Delayed production of [2-^{13}C]lactate and [5-^{13}C]glutamate relative to the substrate peak confirms downstream metabolism in the TCA cycle in our studies. In the future, this could be used to probe the metabolic reprogramming associated with the IDH1 mutation in LGGs wherein we expect greater flux via the TCA and consequent glutamate production when compared to wild-type IDH GBM tumors.

In the case of [1-^{13}C]αKG, we compared two different tumor models: mutant IDH1 BT257 and wild-type IDH1 U87. In contrast to the wild-type IDH1, mutant IDH1 converts αKG into the oncometabolite 2HG.[3,58] Since [5-^{13}C]αKG (184 ppm) and [1-^{13}C]2HG (183.9 ppm) are only 0.1 ppm apart, these two peaks overlap at the 3T field strength used in our study. Therefore, we simultaneously quantified the combined peak at the 184 ppm peak ([5-^{13}C]αKG + [1-^{13}C]2HG). Importantly, however, using our data analysis pipeline we observed a significant increase in the intensity of the 184ppm peak at 38 s in the BT257 IDH1 mutant tumors whereas in the IDH1 wild-type U87 model we only observed a monotonic signal decay. We also detected the production of [1-^{13}C]glutamate which shows a trend toward significance (see Fig 7B and C). This was more clearly observed in the U87 model in which [1-^{13}C]αKG is only converted to [1-^{13}C]glutamate. Our findings are consistent with the expected metabolism of [5-^{13}C]αKG and previous reports[3,29] and highlight the value of our data acquisition and analysis approach for the rapid detection of tumor metabolism. One point warranting further discussion is the denoising performance. Judging from the error bars of the [5-^{13}C]αKG + [1-^{13}C]2HG (see Figure 7B and C), the SVD denoising showed superior performance in the BT257 model compared to the U87 model. However, since the sample sizes are relatively small, investigating the reason for the different denoising performance between tumor models is beyond the scope of this work.

In summary, we describe a comprehensive pipeline that includes acquisition and quantification methods for HP ^{13}C MR spectroscopy using two emerging substrates: [2-^{13}C]pyruvate and [1-^{13}C]αKG. The acquisition approaches including multiband excitation and VFA schemes together with quantification approaches including SVD denoising, LCModel fitting, and VFA correction provided good performance to monitor *in vivo* metabolism. Further studies are needed, but we believe this approach could be used more broadly both in the preclinical and clinical settings to assess the metabolic fate of a range of metabolites.

Supplementary Material

Refer to Web version on PubMed Central for supplementary material.

Acknowledgment

This work was supported by NIH R01CA172845, NIH R01CA197254, NIH P01CA118816, UCSF LOGLIO collective, UCSF NICO project, NIH P30CA082103 HDFCCC cancer imaging resources (CIR), NIH R01CA239288, Department of Defense W81XWH201055315, NIH P41EB013598 Hyperpolarized MRI Technology Resource Center Grant, and American Cancer Society Research Scholar Grant 131715-RSG-18-005-01-CCE.

References

1. Ardenkjær-Larsen JH, Fridlund B, Gram A, et al. Increase in signal-to-noise ratio of> 10,000 times in liquid-state NMR. Proceedings of the National Academy of Sciences. 2003;100(18):10158–10163.
2. Kurhanewicz J, Vigneron DB, Ardenkjær-Larsen JH, et al. Hyperpolarized 13C MRI: path to clinical translation in oncology. Neoplasia. 2019;21(1):1–16. [PubMed: 30472500]
3. Chaumeil MM, Larson PE, Yoshihara HA, et al. Non-invasive in vivo assessment of IDH1 mutational status in glioma. Nature communications. 2013;4(1):1–12.
4. Viswanath P, Najac C, Izquierdo JL, et al. Mutant IDH1 expression is associated with down-regulation of monocarboxylate transporters. Oncotarget. 2016;7(23):34942. [PubMed: 27144334]
5. Izquierdo-Garcia JL, Viswanath P, Eriksson P, et al. IDH1 Mutation Induces Reprogramming of Pyruvate Metabolism. Cancer Res. 2015;75(15):2999–3009. [PubMed: 26045167]
6. Hesketh RL, Brindle KM. Magnetic resonance imaging of cancer metabolism with hyperpolarized (13)C-labeled cell metabolites. Current opinion in chemical biology. 2018;45:187–194. [PubMed: 30007214]
7. Park JM, Josan S, Jang T, et al. Volumetric spiral chemical shift imaging of hyperpolarized [2-13c] pyruvate in a rat c6 glioma model. Magnetic resonance in medicine. 2016;75(3):973–984. [PubMed: 25946547]
8. Xu Y, Ringgaard S, Mariager CØ, et al. Hyperpolarized 13C magnetic resonance imaging can detect metabolic changes characteristic of penumbra in ischemic stroke. Tomography. 2017;3(2):67. [PubMed: 30042973]
9. Cunningham CH, Lau JY, Chen AP, et al. Hyperpolarized 13C metabolic MRI of the human heart: initial experience. Circulation research. 2016;119(11):1177–1182. [PubMed: 27635086]
10. Rider OJ, Apps A, Miller JJ, et al. Noninvasive in vivo assessment of cardiac metabolism in the healthy and diabetic human heart using hyperpolarized 13C MRI. Circulation Research. 2020;126(6):725–736. [PubMed: 32078413]
11. Warburg O. On respiratory impairment in cancer cells. Science. 1956;124:269–270. [PubMed: 13351639]
12. Park I, Hu S, Bok R, et al. Evaluation of heterogeneous metabolic profile in an orthotopic human glioblastoma xenograft model using compressed sensing hyperpolarized 3D 13C magnetic resonance spectroscopic imaging. Magnetic resonance in medicine. 2013;70(1):33–39. [PubMed: 22851374]
13. Rodrigues TB, Serrao EM, Kennedy BW, Hu D-E, Kettunen MI, Brindle KM. Magnetic resonance imaging of tumor glycolysis using hyperpolarized 13 C-labeled glucose. Nature medicine. 2014;20(1):93–97.
14. Park JM, Josan S, Grafendorfer T, et al. Measuring mitochondrial metabolism in rat brain in vivo using MR Spectroscopy of hyperpolarized [2-13C] pyruvate. NMR in biomedicine. 2013;26(10):1197–1203. [PubMed: 23553852]
15. Cabella C, Karlsson M, Canape C, et al. In vivo and in vitro liver cancer metabolism observed with hyperpolarized [5–13C] glutamine. Journal of magnetic resonance. 2013;232:45–52. [PubMed: 23689113]

16. Molloy AR, Najac C, Viswanath P, et al. MR-detectable metabolic biomarkers of response to mutant IDH inhibition in low-grade glioma. Theranostics. 2020;10(19):8757–8770. [PubMed: 32754276]
17. Park JM, Spielman DM, Josan S, et al. Hyperpolarized 13C-lactate to 13C-bicarbonate ratio as a biomarker for monitoring the acute response of anti-vascular endothelial growth factor (anti-VEGF) treatment. NMR in Biomedicine. 2016;29(5):650–659. [PubMed: 26990457]
18. Chen AP, Chu W, Gu Y-P, Cunnhingham CH. Probing early tumor response to radiation therapy using hyperpolarized [1–13 C] pyruvate in MDA-MB-231 xenografts. PLoS One. 2013;8(2):e56551. [PubMed: 23424666]
19. Nelson SJ, Kurhanewicz J, Vigneron DB, et al. Metabolic imaging of patients with prostate cancer using hyperpolarized [1–13C] pyruvate. Science translational medicine. 2013;5(198):198ra108–198ra108.
20. Chen H-Y, Aggarwal R, Bok RA, et al. Hyperpolarized 13 C-pyruvate MRI detects real-time metabolic flux in prostate cancer metastases to bone and liver: a clinical feasibility study. Prostate cancer and prostatic diseases. 2020;23(2):269–276. [PubMed: 31685983]
21. Chung BT, Chen H-Y, Gordon J, et al. First hyperpolarized [2–13C] pyruvate MR studies of human brain metabolism. Journal of Magnetic Resonance. 2019;309:106617. [PubMed: 31648132]
22. Topping GJ, Hundshammer C, Nagel L, et al. Acquisition strategies for spatially resolved magnetic resonance detection of hyperpolarized nuclei. Magnetic Resonance Materials in Physics, Biology and Medicine. 2020;33(2):221–256.
23. Gordon JW, Chen HY, Dwork N, Tang S, Larson PE. Fast Imaging for Hyperpolarized MR Metabolic Imaging. Journal of Magnetic Resonance Imaging. 2020.
24. Daniels CJ, McLean MA, Schulte RF, et al. A comparison of quantitative methods for clinical imaging with hyperpolarized (13)C-pyruvate. NMR Biomed. 2016;29(4):387–399. [PubMed: 27414749]
25. Larson PE, Chen HY, Gordon JW, et al. Investigation of analysis methods for hyperpolarized 13C-pyruvate metabolic MRI in prostate cancer patients. NMR in Biomedicine. 2018;31(11):e3997. [PubMed: 30230646]
26. Ward CS, Venkatesh HS, Chaumeil MM, et al. Noninvasive detection of target modulation following phosphatidylinositol 3-kinase inhibition using hyperpolarized 13C magnetic resonance spectroscopy. Cancer research. 2010;70(4):1296–1305. [PubMed: 20145128]
27. Viswanath P, Radoul M, Izquierdo-Garcia JL, et al. Mutant IDH1 gliomas downregulate phosphocholine and phosphoethanolamine synthesis in a 2-hydroxyglutarate-dependent manner. Cancer & metabolism. 2018;6(1):3. [PubMed: 29619216]
28. Radoul M, Chaumeil MM, Eriksson P, Wang AS, Phillips JJ, Ronen SM. MR studies of glioblastoma models treated with dual PI3K/mTOR inhibitor and temozolomide: metabolic changes are associated with enhanced survival. Molecular cancer therapeutics. 2016;15(5):1113–1122. [PubMed: 26883274]
29. Chaumeil MM, Larson PE, Woods SM, et al. Hyperpolarized [1–13C] glutamate: a metabolic imaging biomarker of IDH1 mutational status in glioma. Cancer research. 2014;74(16):4247–4257. [PubMed: 24876103]
30. Lau AZ, Chen AP, Hurd RE, Cunningham CH. Spectral–spatial excitation for rapid imaging of DNP compounds. NMR in Biomedicine. 2011;24(8):988–996. [PubMed: 21751271]
31. Larson PE, Kerr AB, Chen AP, et al. Multiband excitation pulses for hyperpolarized 13C dynamic chemical-shift imaging. Journal of magnetic resonance (San Diego, Calif : 1997). 2008;194(1):121–127.
32. Maidens J, Gordon JW, Arcak M, Larson PE. Optimizing flip angles for metabolic rate estimation in hyperpolarized carbon-13 MRI. IEEE transactions on medical imaging. 2016;35(11):2403–2412. [PubMed: 27249825]
33. Xing Y, Reed GD, Pauly JM, Kerr AB, Larson PE. Optimal variable flip angle schemes for dynamic acquisition of exchanging hyperpolarized substrates. Journal of magnetic resonance. 2013;234:75–81. [PubMed: 23845910]

34. Smith LM, Wade TP, Friesen-Waldner LJ, McKenzie CA. Optimizing SNR for multi-metabolite hyperpolarized carbon-13 MRI using a hybrid flip-angle scheme. Magnetic resonance in medicine. 2020;84(3):1510–1517. [PubMed: 32011018]
35. Batsios G, Najac C, Cao P, et al. In vivo detection of γ-glutamyl-transferase up-regulation in glioma using hyperpolarized γ-glutamyl-[1–13 C] glycine. Scientific reports. 2020;10(1):1–10. [PubMed: 31913322]
36. Izquierdo-Garcia JL, Viswanath P, Eriksson P, et al. Metabolic reprogramming in mutant IDH1 glioma cells. PloS one. 2015;10(2):e0118781. [PubMed: 25706986]
37. Mazor T, Chesnelong C, Pankov A, et al. Clonal expansion and epigenetic reprogramming following deletion or amplification of mutant IDH1. Proceedings of the National Academy of Sciences. 2017;114(40):10743–10748.
38. Larson PE. Hyperpolarized-MRI-Toolbox. DOI: 10.5281/zenodo.1198915 Available online at: https://github.com/LarsonLab/hyperpolarized-mri-toolbox 2020.
39. Nagashima K. Optimum pulse flip angles for multi-scan acquisition of hyperpolarized NMR and MRI. Journal of Magnetic Resonance. 2008;190(2):183–188. [PubMed: 18023219]
40. Provencher SW. Automatic quantitation of localized in vivo 1H spectra with LCModel. NMR in Biomedicine: An International Journal Devoted to the Development and Application of Magnetic Resonance In Vivo. 2001;14(4):260–264.
41. Provencher SW. Estimation of metabolite concentrations from localized in vivo proton NMR spectra. Magnetic resonance in medicine. 1993;30(6):672–679. [PubMed: 8139448]
42. Henry E, Hofrichter J. [8] Singular value decomposition: Application to analysis of experimental data. In: Methods in enzymology. Vol 210. Elsevier; 1992:129–192.
43. Macovski A. Noise in MRI. Magnetic resonance in medicine. 1996;36(3):494–497. [PubMed: 8875425]
44. Holden J, Halama J, Hasegawa B. The propagation of stochastic pixel noise into magnitude and phase values in the Fourier analysis of digital images. Physics in Medicine & Biology. 1986;31(4):383. [PubMed: 3737679]
45. Bernstein MA, Thomasson DM, Perman WH. Improved detectability in low signal-to-noise ratio magnetic resonance images by means of a phase-corrected real reconstruction. Medical Physics. 1989;16(5):813–817. [PubMed: 2811764]
46. Datta K, Spielman DM. Doublet asymmetry for estimating polarization in hyperpolarized 13C–pyruvate studies. NMR in Biomedicine. 2017;30(2):e3670.
47. Batsios G, Najac C, Cao P, et al. In vivo detection of γ-glutamyl-transferase up-regulation in glioma using hyperpolarized γ-glutamyl-[1–13C]glycine. Scientific reports. 2020;10(1):6244. [PubMed: 32277103]
48. Mazuel L, Schulte RF, Cladière A, et al. Intracerebral synthesis of glutamine from hyperpolarized glutamate. Magn Reson Med. 2017;78(4):1296–1305. [PubMed: 27851869]
49. Hu S, Yoshihara HA, Bok R, et al. Use of hyperpolarized [1–13C] pyruvate and [2–13C] pyruvate to probe the effects of the anticancer agent dichloroacetate on mitochondrial metabolism in vivo in the normal rat. Magnetic resonance imaging. 2012;30(10):1367–1372. [PubMed: 22819176]
50. Wagshul ME, Button TM, Li HF, et al. In vivo MR imaging and spectroscopy using hyperpolarized 129Xe. Magnetic resonance in medicine. 1996;36(2):183–191. [PubMed: 8843370]
51. Brender JR, Kishimoto S, Merkle H, et al. Dynamic imaging of glucose and lactate metabolism by 13 C-MRS without hyperpolarization. Scientific reports. 2019;9(1):1–14. [PubMed: 30626917]
52. Chen HY, Autry AW, Brender JR, et al. Tensor image enhancement and optimal multichannel receiver combination analyses for human hyperpolarized 13C MRSI. Magnetic Resonance in Medicine. 2020.
53. Henry PG, Öz G, Provencher S, Gruetter R. Toward dynamic isotopomer analysis in the rat brain in vivo: automatic quantitation of 13C NMR spectra using LCModel. NMR in Biomedicine: An International Journal Devoted to the Development and Application of Magnetic Resonance In Vivo. 2003;16(6-7):400–412.
54. Deelchand DK, Nguyen TM, Zhu XH, Mochel F, Henry PG. Quantification of in vivo 31P NMR brain spectra using LCModel. NMR in Biomedicine. 2015;28(6):633–641. [PubMed: 25871439]
55. Provencher SW. LCModel & LCMgui user's manual. LCModel Version. 2014:6–2.

56. Hong D, van Asten JJ, Rankouhi SR, Thielen J-W, Norris DG. Effect of linewidth on estimation of metabolic concentration when using water lineshape spectral model fitting for single voxel proton spectroscopy at 7 T. Journal of Magnetic Resonance. 2019;304:53–61. [PubMed: 31102923]

57. De Graaf RA. In vivo NMR spectroscopy: principles and techniques. John Wiley & Sons; 2019.

58. Ronen SM, Izquierdo-Garcia JL, Chaumeil MM, Cai LM, Phillips JJ, Pieper RO. Metabolic Imaging Biomarkers For Mutant Idh1 Gliomas. Neuro-oncology. 2014;16(Suppl 3):iii12.

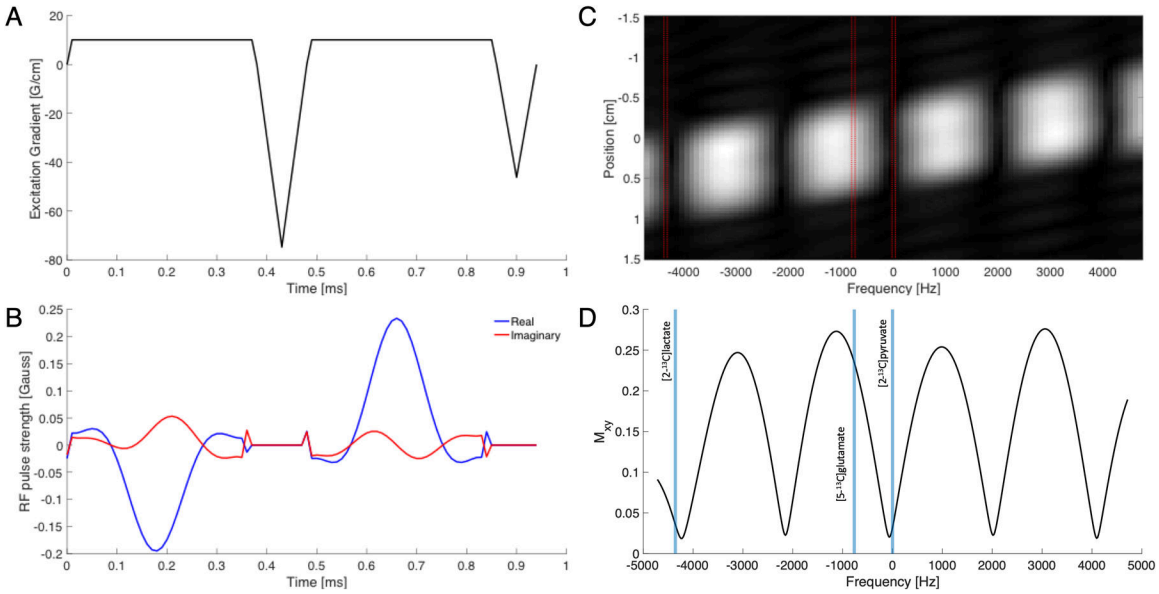

Figure 1.

Spectral-spatial RF excitation pulse with independent flip angle control over two excitation bands. (A and B) gradient and RF waveforms (blue is real and red is imaginary part of the RF pulse). This 0.93 ms pulse was designed for a 10 mm slab, with the following resonances and their corresponding bandwidths and flip angles: 207.8 ppm ± 1 ppm ([2-^{13}C]pyruvate), 4°; 183.9 ppm ± 1 ppm ([5-^{13}C]glutamate), 30°. (C) The magnitude of the spectral-spatial profile of the pulse at different shifts from the iso-center and over a range of frequencies. (D) Spectral profile at the center of the slab (at 0 cm).

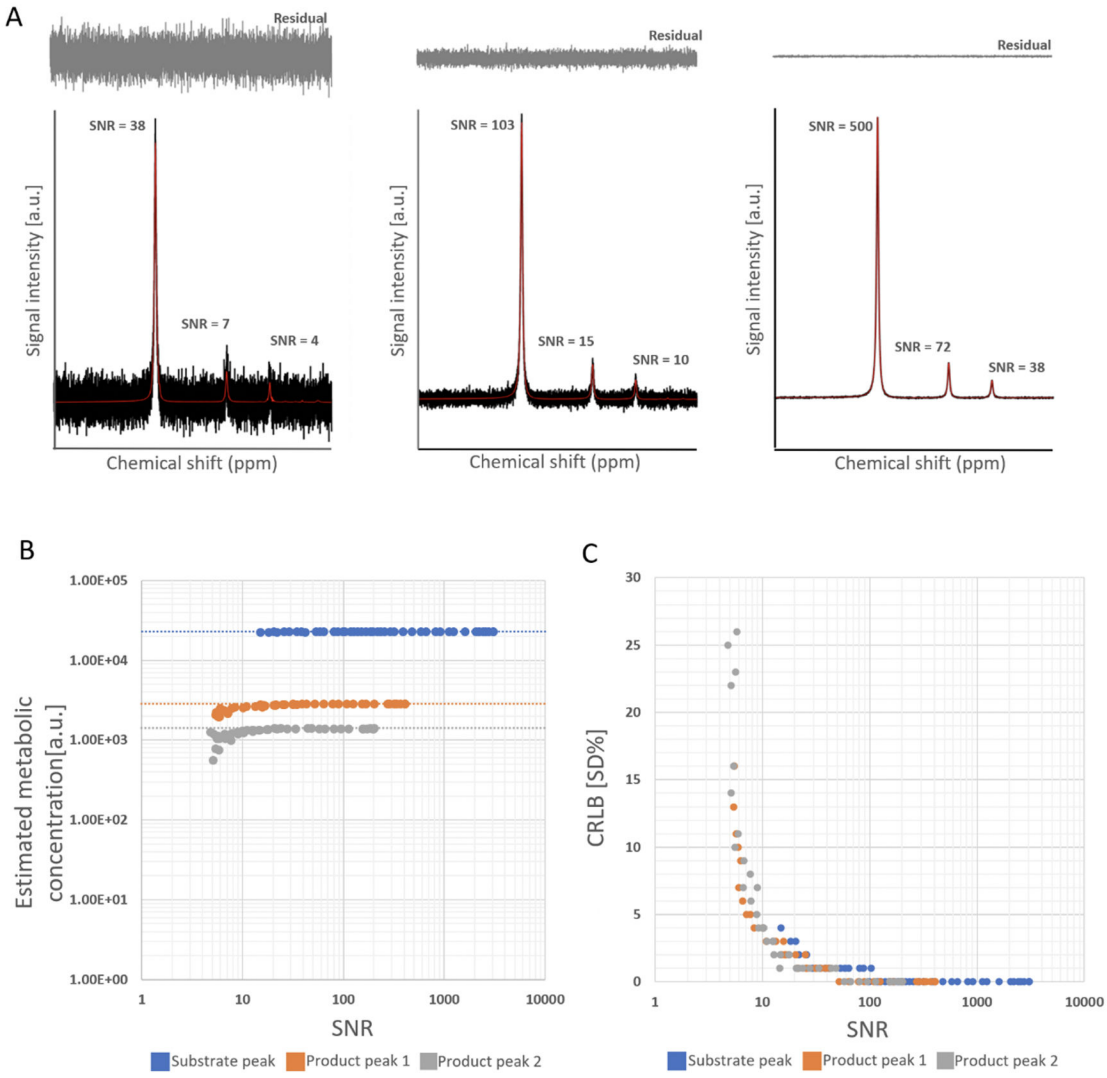

Figure 2.

LCModel results for simulated spectra of different SNR levels (A). Quantified concentrations (B) and corresponding CRLBs (C) for simulated spectra with various SNRs. Note that dotted lines on Figure2B indicate true concentrations of each metabolite. As SNR increases, estimated concentrations are converging to their true concentrations.

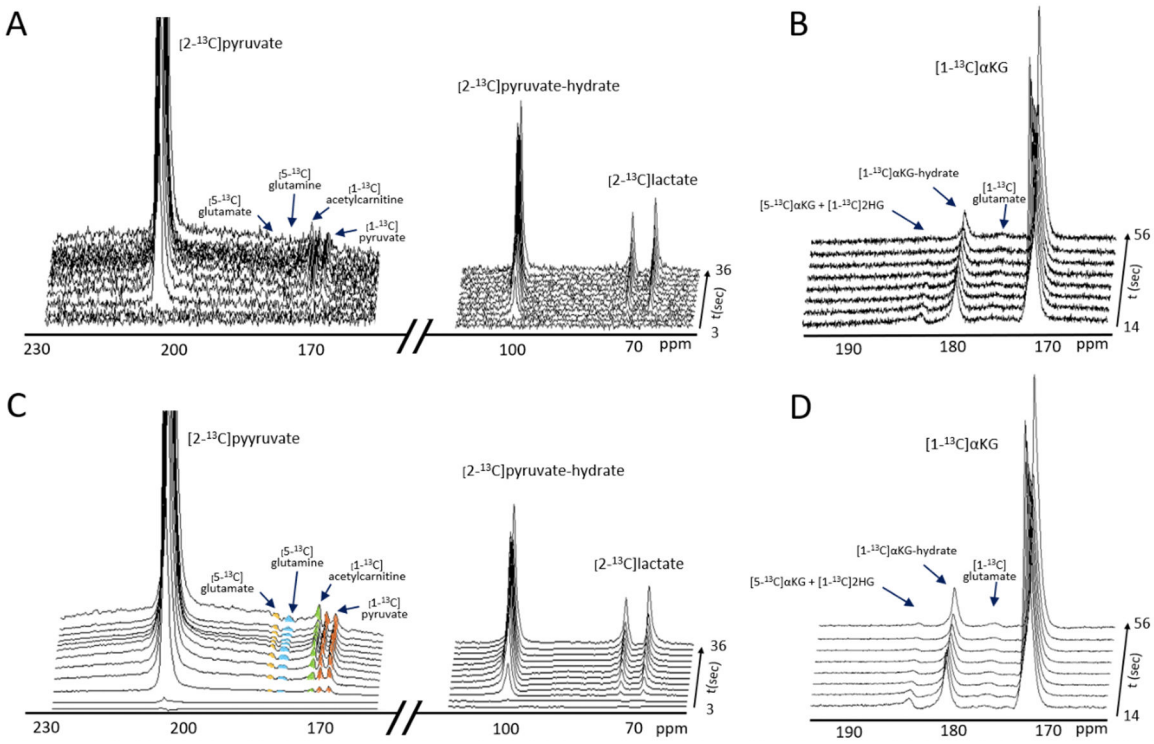

Figure 3.

A comparison of *in vivo* spectra between pre- (A and B) and post-denoising (C and D) using the SVD and following [2-^{13}C]pyruvate injection (A and C) and [1-^{13}C]α-ketoglutarate injection (B and D). After denoising, lower concentration product signals are more clearly visible (C and D).

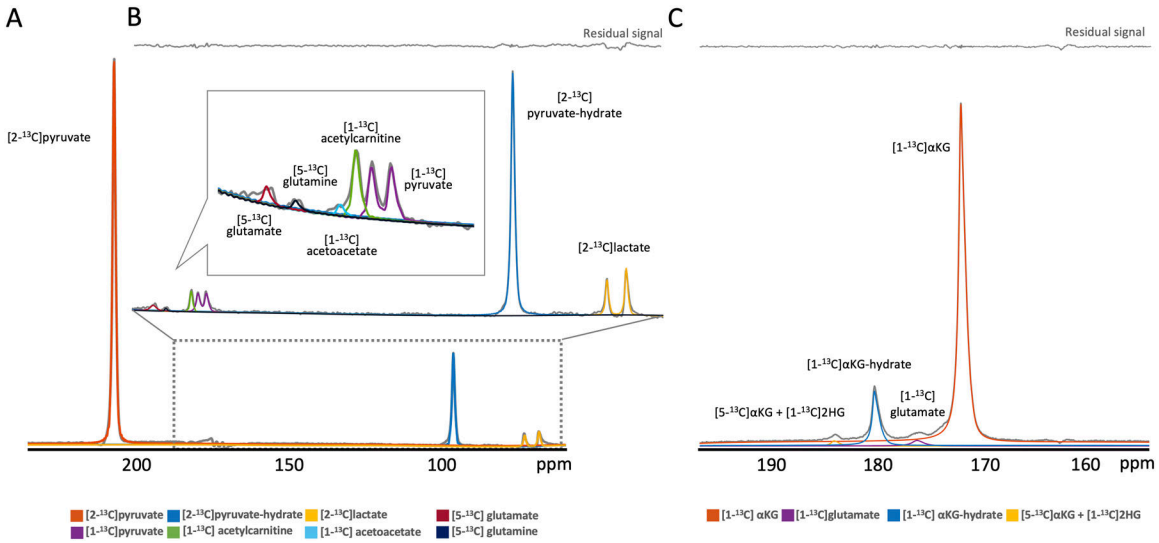

Figure 4.

Examples of *in vivo* spectra following [2-^{13}C]pyruvate (A and B) and [1-^{13}C]αKG (C) injections with individual metabolite fitting lines. (A): [2-^{13}C]pyruvate (orange), [2-^{13}C]pyruvate-hydrate (blue), and [2-^{13}C]lactate (yellow). (B): [5-^{13}C]glutamate (red), [5-^{13}C]glutamine (navy), [1-^{13}C]acetoacetate (light blue), [1-^{13}C]acetylcarnitine (green), [1-^{13}C]pyruvate (purple), and residual signal (above). Note that Figure 4B shows the fitting result after excluding [2-^{13}C]pyruvate to enable phasing of all metabolite. (C): [5-^{13}C]α-ketoglutarate + [1-^{13}C]2-hydroxyglutarate (yellow), [1-^{13}C]α-ketoglutarate-hydrate (blue), [1-^{13}C]glutamate (purple), [1-^{13}C]α-ketoglutarate (orange), and residual signal (above).

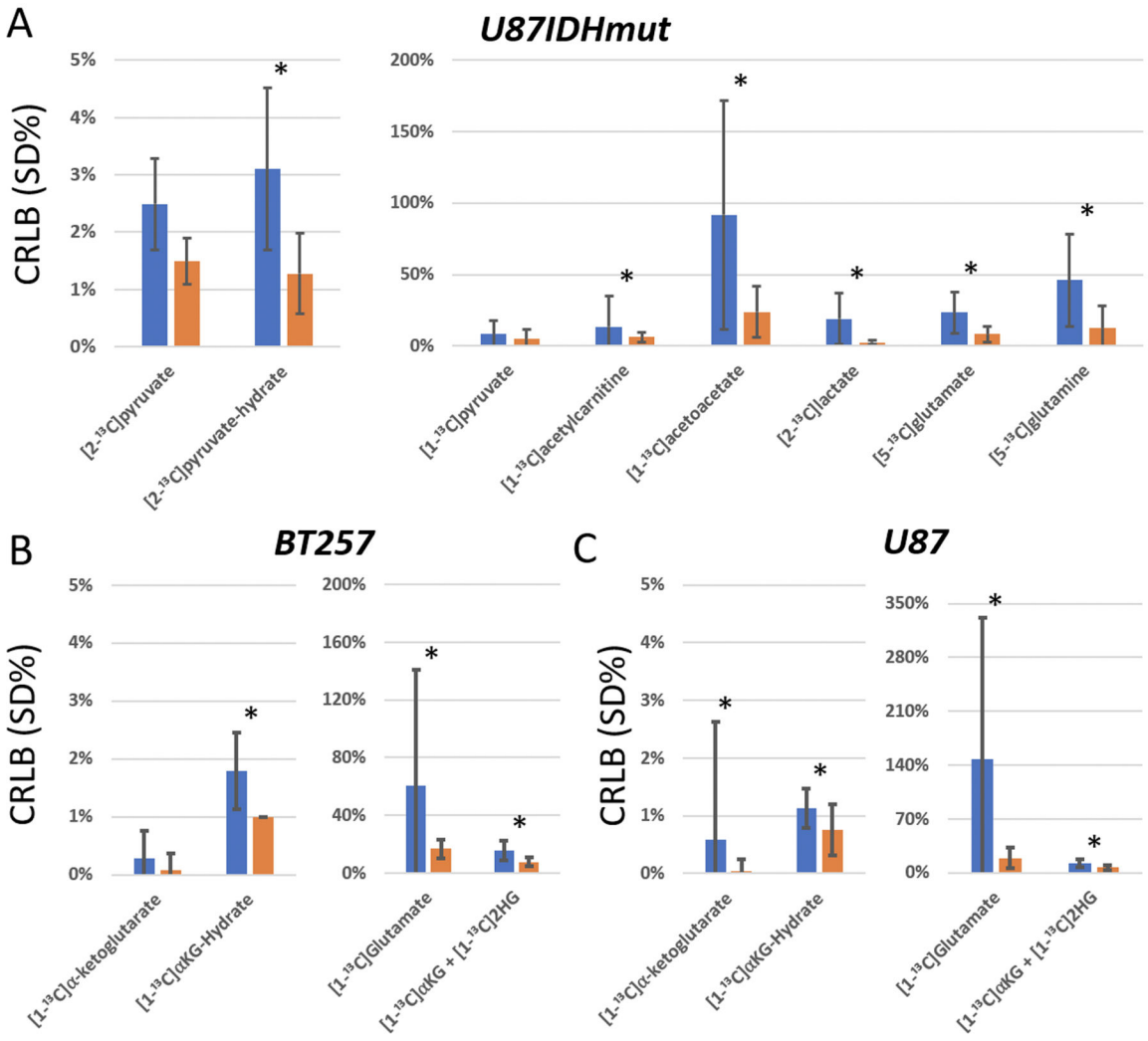

Figure 5.

Comparison of the mean CRLB over all time points between the pre- (blue) and post-denoised (orange) results for [2-^{13}C]pyruvate (A: U87IDHmut tumors), [1-^{13}C]α-ketoglutarate (B: BT257 and C: U87 tumors). Error bars indicate 95% confidence intervals and asterisks indicate a significant difference between the two groups: $p<0.05$.

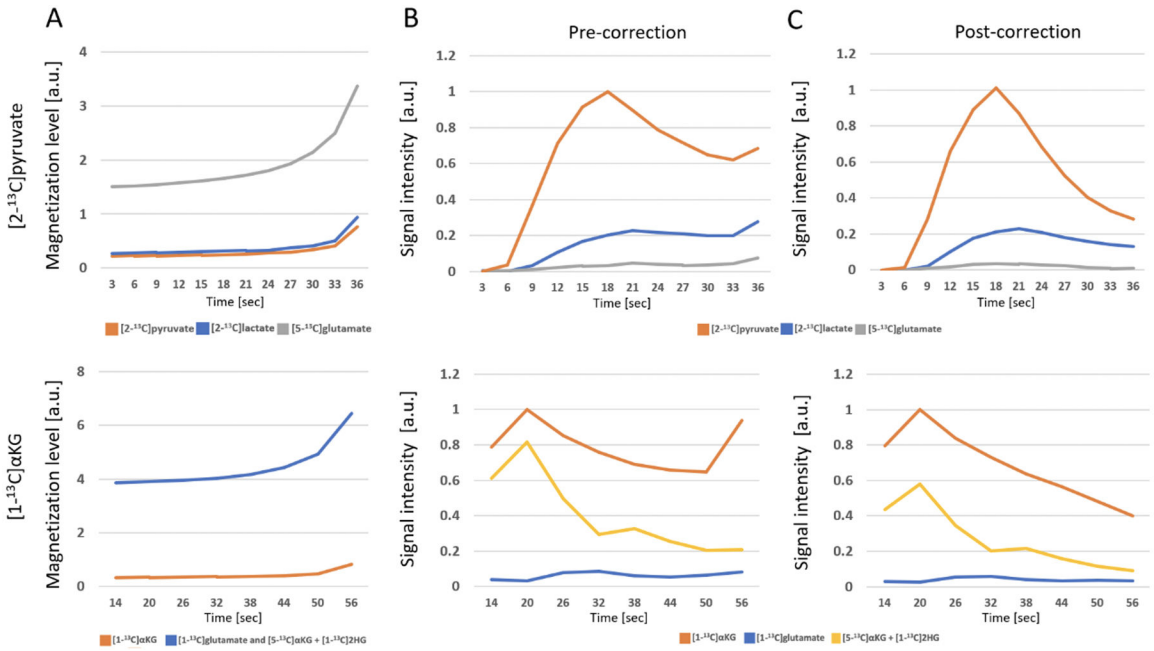

Figure 6.

(A) Expected magnetization variations over flip angles determined by quantum mechanical calculation for each RF pulse for the metabolites observed following [2-^{13}C]pyruvate (upper panel) and [1-^{13}C]α-ketoglutarate (lower panel) injections. Example of pre- (B) and post-VFA correction (C) for metabolite concentrations quantified by LCModel for [2-^{13}C]pyruvate (upper panels) and [1-^{13}C]α-ketoglutarate (lower panels) injections. The correction results in metabolite dynamic curves that reflect the expected increase due to metabolic conversion followed by a decrease due to magnetization decay. Note that metabolite signals in Figures 6B and 6C were normalized to the maximum substrate signal to compare the correction effect directly. Note that time indicates the elapsed time after starting the substate injection.

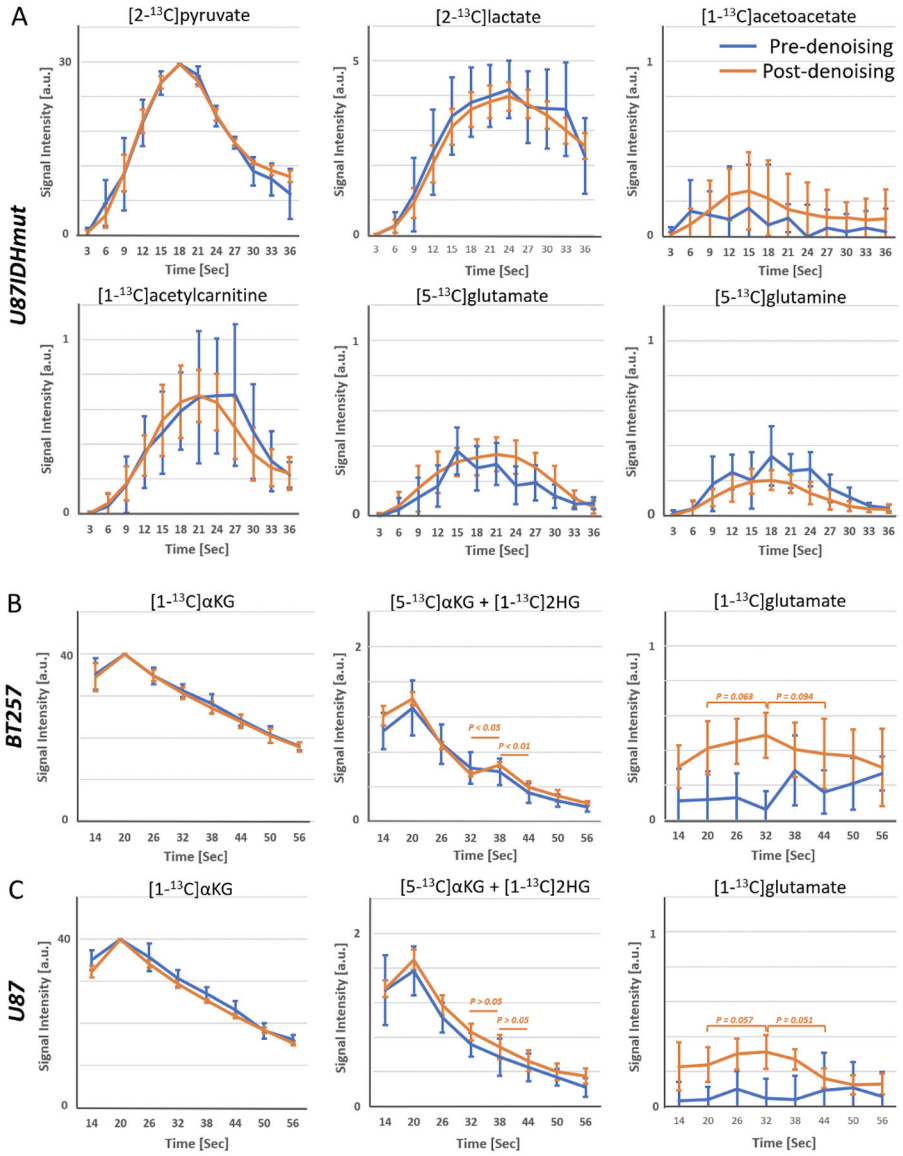

Figure 7.

Averaged metabolic kinetics following LCModel fitting and VFA correction based on spectra pre-denoising (blue) and post-denoising (orange) for [2-^{13}C]pyruvate (A: U87IDHmut model) and [1-^{13}C]α-ketoglutarate (B: BT257 and C: U87 models). For the BT257 model, the [5-^{13}C]αKG + [1-^{13}C]2HG peak was significantly increased at 38 s, whereas, the U87 model did not show this second peak. Note the error bars indicate standard deviations.